The Astrophysical Journal, 599:1116–1128, 2003 December 20

MAGNETIC FIELDS IN COOL CLOUDS WITHIN THE CENTRAL 50 PARSECS OF THE GALAXY

David T. Chuss
NASA Goddard Space Flight Center, Code 685, Greenbelt, MD 20771; and Northwestern University; chuss@stars.gsfc.nasa.gov
Jacqueline A. Davidson and Jessie L. Dotson
NASA Ames Research Center, Moffett Field, CA 94035
C. Darren Dowell
California Institute of Technology, Pasadena, CA 91125
Roger H. Hildebrand
Enrico Fermi Institute, University of Chicago, 5640 South Ellis Avenue, Chicago, IL 60637
Giles Novak
Department of Physics and Astronomy, Northwestern University, 2131 Tech Drive, Evanston, IL 60208
and
John E. Vaillancourt
University of Wisconsin, Madison, WI 53706
Received 2003 January 3; accepted 2003 September 2

ABSTRACT

We report the detection of polarized emission in the vicinity of the Galactic center for 158 positions within eight different pointings of the Hertz polarimeter operating on the Caltech Submillimeter Observatory. These pointings include locations 2′ offset to the east, northeast, and northwest of M−0.02−0.07; locations to the southeast and northwest of the 20 km s^{-1} cloud (M−0.13−0.08); CO 0.02−0.02, M0.07−0.08; and M0.11−0.08. We use these data in conjunction with previous far-infrared and submillimeter polarization results to find that the direction of the inferred magnetic field is related to the density of the molecular material in the following way: in denser regions, the projected field is generally parallel to the Galactic plane, whereas in regions of lower density, the field is generally perpendicular to the plane. One possible explanation for this result is that an initially poloidal field has been sheared into a toroidal configuration in regions that are dense enough such that the gravitational energy density is greater than the energy density of the magnetic field. Another possibility is that winds due to supernovae in the central molecular zone are responsible for deviations from a toroidal field outside of the densest molecular regions.

Subject headings: dust, extinction — Galaxy: center — ISM: magnetic fields — submillimeter — techniques: polarimetric

1. INTRODUCTION

Despite significant advancement over the last two decades, the Galactic center magnetosphere is still not well understood; however, determining the geometry and strength of the magnetic field in this region is crucial to developing an understanding of the dynamics of the Galactic center. Another reason that the magnetosphere is of interest lies in the Galactic center's role as an active galactic nucleus. In the central engines of galaxies, magnetic fields are believed to be important in angular momentum transport and jet dynamics.

The most striking evidence for the existence of magnetic fields in the Galactic center is the existence of the nonthermal filaments (NTFs) of the Galactic center radio arc (GCRA; Yusef-Zadeh, Morris, & Chance 1984). Radio polarization measurements have confirmed the synchrotron nature of the emission from these filaments and support the notion that the filaments trace magnetic field lines (Tsuboi et al. 1986). Almost all of the confirmed NTFs that have been discovered in the Galactic center region are aligned with their long axes within 20° of perpendicular to the plane of the Galaxy (LaRosa et al. 2000). The presence of these filaments has led to the idea that these filaments trace the inner part of a dipole or *poloidal* magnetic field.

In many cases NTFs are observed to be interacting with Galactic center molecular clouds. The best example of this is in the center of the GCRA, where the 25 km s^{-1} molecular cloud associated with G0.18−0.04 (the Sickle) is coincident with the filaments (Serabyn & Güsten 1991). The lack of observed distortion of the filaments allows one to set a lower limit for the strength of the magnetic field. This argument yields $B >$ a few mG (Yusef-Zadeh & Morris 1987a, 1987b). The association of molecular clouds with NTFs has motivated the idea that the generation of the relativistic electrons required to create these NTFs could occur as a result of a molecular cloud/magnetic flux-tube interaction. The specific mechanism thought to be responsible for the generation of these relativistic electrons is magnetic reconnection between the fields in the flux tube and those in the cloud (Serabyn & Morris 1994; for a review, see Davidson 1996).

Magnetically aligned dust grains emit polarized radiation in the far-infrared and submillimeter. Thus, polarimetry at these wavelengths has proven to be a reliable technique for measuring the magnetic field configuration, projected into the plane of the sky and integrated along the line of sight. Previous polarimetry data have shown that the field in the dense molecular clouds is not generally consistent with the poloidal field traced by the filaments. Novak et al. (2000) have shown that in the molecular cloud M−0.13−0.08, the field is nearly parallel to the Galactic plane, indicating that gravitational rotation and infall have sheared out the field into a *toroidal* configuration. In addition, 60 μm polarimetry of the molecular cloud associated with the Sickle indicates that the field in this region is parallel to the Galactic plane (Dotson et al. 2000).

Uchida, Shibata, & Sofue (1985) have constructed a model that connects poloidal and toroidal fields. Because the magnetic flux is frozen into the matter, differential rotation and infall can shear an initially poloidal field into a toroidal one in sufficiently dense regions of the Galactic center. Novak et al. (2003) have shown that on large scales, the dust in the central molecular zone (CMZ) of the Galaxy is permeated by a field that is oriented in a direction parallel to the plane of the Galaxy. They compare their observation to the spatial distribution of the direction of Faraday rotation in the Galactic center and show that these two different techniques for measuring fields yield results that are consistent with the model of Uchida, Shibata, & Sofue (1985).

In this paper we find that the inferred magnetic field direction in the cold dust of the central 50 pc is dependent on the submillimeter flux. In underdense regions, the field aligns with that of the brightest NTFs in a direction perpendicular to the plane. In overdense regions, however, the field has a toroidal geometry. We consider two possible explanations for this result. The first is that the field in the dust is generally toroidal, but turbulence introduced by explosions in the Galactic center has caused deviations from a toroidal field in the underdense regions.

The second possibility involves extending the ideas that underlie the model of Uchida et al. (1985) to the inner 50 pc of the Galactic center. In this case, the vertical field found in the underdense regions is associated with the poloidal field of the NTFs. In these underdense regions, there is insufficient mass to distort this initially poloidal field. However, in dense molecular clouds, the gravitational energy density is strong enough to distort the initial field configuration into a toroidal magnetic field structure.

Section 2 describes the observations. In § 3 we discuss our interpretation. Finally, our conclusions are summarized in § 4.

2. OBSERVATIONS

The data were obtained using the University of Chicago 32 pixel Hertz polarimeter (Dowell et al. 1998) at the Caltech Submillimeter Observatory (CSO) on Mauna Kea, Hawaii, in April of 2001. The beam size of Hertz is 20″ FWHM with a pixel spacing of 18″. The central wavelength of the Hertz passband is 350 μm with a $\Delta\lambda/\lambda$ of 0.1.

The observing technique used with Hertz involves a combination of high-frequency "chopping," in which the array footprint is alternately pointed at the source and a reference position 6′ away in cross-elevation, and low-frequency "nodding," during which the source is alternately placed in the right- and left-hand beams of the telescope. One undesirable complication that this observational scheme introduces is the problem of polarized flux in the reference beam. This problem is discussed in detail in § 3.4. For a full description of the observing and analysis procedures, see Schleuning et al. (1997) and Dowell et al. (1998).

During the observations, a total of 158 new polarization measurements were obtained, having a polarimetric signal-to-noise ratio greater than 3. These data are given in Tables 1–7.

TABLE 1

M0.13−0.08

$\Delta\alpha$[a] (arcsec)	$\Delta\delta$[a] (arcsec)	P (%)	σ_P	ϕ (deg)	σ_ϕ
−54	72	3.04	1.06	108.1	8.6
−36	72	2.21	0.71	99.1	9.0
−36	90	2.61	0.94	100.2	9.8
−36	108	4.98	1.48	102.4	7.8
18	−54	1.21	0.41	107.3	9.4
36	−54	1.41	0.40	91.3	8.1
54	−36	1.41	0.42	70.5	8.7
72	−90	1.83	0.57	97.4	8.7
72	−54n	2.07	0.48	82.2	6.7
90	−54	2.46	0.57	87.2	6.6
108	−54	2.20	0.70	58.8	9.5

[a] Sky positions are relative to $17^{\mathrm{h}}45^{\mathrm{m}}37^{\mathrm{s}}.30$, $-29^\circ05'39''.78$ (J2000.0).

TABLE 2

CO 0.02−0.02

$\Delta\alpha$[a] (arcsec)	$\Delta\delta$[a] (arcsec)	P (%)	σ_P	ϕ (deg)	σ_ϕ
−54	−18	2.76	0.85	107.6	8.8
−54	18	2.75	0.74	88.5	7.7
−36	−54	3.66	1.14	107.7	9.0
−36	−36	3.17	0.60	103.8	5.4
−36	−18	2.66	0.59	100.2	6.2
−36	0	3.16	0.63	91.3	5.7
−36	18	1.82	0.59	85.4	9.4
−36	36	3.08	0.73	80.3	6.8
−18	−54	3.20	0.89	112.8	8.2
−18	−36	1.46	0.39	98.0	7.7
−18	−18	1.74	0.42	78.5	6.9
−18	0	2.72	0.55	83.2	5.8
−18	18	2.33	0.56	66.4	6.8
−18	36	2.02	0.57	68.9	8.2
−18	54	2.20	0.69	63.2	9.6
0	−36	1.74	0.36	81.8	6.0
0	−18	2.09	0.32	95.2	4.3
0	0	1.13	0.32	75.1	8.2
0	18	1.88	0.43	79.6	6.5
0	36	2.75	0.45	60.7	4.7
0	54	2.47	0.80	79.0	9.6
18	−36	1.33	0.34	79.1	7.2
18	−18	2.13	0.30	91.3	4.1
18	0	1.18	0.27	73.3	6.6
18	18	2.27	0.39	63.7	4.9
18	36	3.08	0.60	76.5	5.7
36	−36	1.71	0.59	75.4	9.9
36	−18	1.69	0.38	68.6	6.5
36	0	1.98	0.30	67.6	4.3
36	18	2.43	0.52	63.5	6.3
36	36	3.53	0.85	67.7	7.0
54	−18	2.23	0.75	58.7	9.8
54	0	3.22	0.70	63.3	6.9

[a] Sky positions are relative to $17^{\mathrm{h}}45^{\mathrm{m}}42^{\mathrm{s}}.10$, $-28^\circ56'5''.1$ (J2000.0).

TABLE 3

NORTHWEST OF M0.02−0.07

$\Delta\alpha^{a}$ (arcsec)	$\Delta\delta^{a}$ (arcsec)	P (%)	σ_P	ϕ (deg)	σ_ϕ
−54	0	2.13	0.51	102.8	7.1
−54	36	1.68	0.47	80.7	8.0
−36	18	0.97	0.32	83.0	9.4
−36	36	1.45	0.40	79.0	7.8
−18	−36	2.05	0.41	92.9	5.8
−18	0	1.46	0.46	78.9	8.9
−18	36	2.01	0.46	61.9	6.4
0	36	1.33	0.46	73.3	9.7
18	−36	1.07	0.30	60.8	7.8
18	0	1.36	0.34	56.4	7.1
18	18	1.63	0.37	55.5	6.4
18	36	1.49	0.48	60.6	9.0
18	54	2.60	0.73	64.3	7.8
36	−36	0.98	0.34	66.7	9.7
36	−18	1.50	0.31	50.5	5.9
36	0	1.12	0.33	45.5	8.4
36	18	2.31	0.36	58.0	4.3
36	36	2.22	0.47	58.9	6.1
54	−36	2.56	0.80	52.2	9.0

[a] Sky positions are relative to $17^{\mathrm{h}}45^{\mathrm{m}}46\overset{\mathrm{s}}{.}7$, $-28^{\circ}57'30\overset{''}{.}0$ (J2000.0).

TABLE 4

NORTHEAST OF M0.02−0.07

$\Delta\alpha^{a}$ (arcsec)	$\Delta\delta^{a}$ (arcsec)	P (%)	σ_P	ϕ (deg)	σ_ϕ
−54	−18	0.84	0.26	68.8	9.1
−54	0	0.78	0.24	62.0	8.8
−54	18	1.33	0.23	55.8	5.0
−54	36	1.27	0.33	43.8	7.5
−36	−18	0.88	0.23	53.1	7.5
−36	18	1.17	0.21	37.2	5.0
−36	36	0.81	0.22	38.1	7.4
−36	54	1.13	0.35	48.7	9.1
−18	−36	1.52	0.22	57.9	4.4
−18	−18	1.46	0.23	43.4	4.5
−18	0	1.28	0.25	42.5	5.6
−18	18	1.46	0.37	42.2	7.2
−18	36	1.70	0.28	29.2	4.5
−18	54	2.35	0.36	42.7	4.4
0	−36	1.44	0.25	54.6	5.2
0	−18	1.58	0.26	41.0	4.6
0	0	1.58	0.26	39.5	4.7
0	18	1.92	0.42	29.4	5.8
0	36	1.99	0.40	44.0	5.7
0	54	2.16	0.45	47.3	6.0
18	−54	2.30	0.55	65.5	7.2
18	−36	1.08	0.30	41.1	7.9
18	−18	1.13	0.33	44.5	8.4
18	0	1.90	0.41	25.7	5.8
18	18	1.75	0.46	38.0	7.4
18	36	2.94	0.65	34.3	6.1
18	54	3.25	0.72	49.4	6.5
36	−36	1.81	0.51	45.0	8.1
36	−18	1.20	0.44	20.7	9.9
36	18	3.30	0.60	29.0	5.0
54	0	4.63	1.09	37.7	7.0
54	18	6.69	1.41	32.9	6.0

[a] Sky positions are relative to $17^{\mathrm{h}}45^{\mathrm{m}}55\overset{\mathrm{s}}{.}0$, $-28^{\circ}57'29\overset{''}{.}7$ (J2000.0).

TABLE 5

EAST OF M0.02−0.07

$\Delta\alpha^{a}$ (arcsec)	$\Delta\delta^{a}$ (arcsec)	P (%)	σ_P	ϕ (deg)	σ_ϕ
−54	−36	1.49	0.31	58.5	6.5
−54	−18	1.03	0.18	49.7	5.1
−54	0	1.26	0.16	49.3	3.5
−54	18	1.18	0.16	53.7	3.9
−54	36	1.44	0.26	53.0	5.0
−36	−54	1.38	0.38	54.7	8.1
−36	−36	1.30	0.22	43.5	4.8
−36	−18	0.67	0.18	47.3	7.6
−36	0	0.71	0.17	43.8	6.6
−36	18	0.80	0.16	39.1	5.8
−36	36	1.60	0.21	35.2	3.6
−36	54	1.34	0.38	41.3	8.2
−18	−54	2.38	0.56	34.4	6.5
−18	−18	0.59	0.19	37.5	9.2
−18	18	1.18	0.24	24.2	5.9
−18	36	2.15	0.23	36.1	3.0
−18	54	1.44	0.39	25.2	8.1
0	−54	2.25	0.64	51.1	8.2
0	−36	1.82	0.30	37.3	4.7
0	−18	1.52	0.21	31.0	4.0
0	0	1.15	0.21	39.6	5.1
0	18	1.94	0.26	37.9	3.8
0	36	2.53	0.32	28.0	3.6
0	54	2.27	0.56	37.6	7.3
18	−18	1.27	0.25	27.6	5.5
18	0	0.94	0.27	34.2	8.3
18	18	2.13	0.34	34.1	4.7
18	36	3.25	0.52	38.4	4.6
18	54	3.55	0.79	31.2	6.7
36	−18	1.61	0.35	29.8	6.4
36	0	2.25	0.38	39.7	4.9
36	18	2.48	0.45	39.1	5.2
36	36	4.00	1.19	41.0	8.6

[a] Sky positions are relative to $17^{\mathrm{h}}45^{\mathrm{m}}59\overset{\mathrm{s}}{.}3$, $-28^{\circ}59'4\overset{''}{.}5$ (J2000.0).

TABLE 6

M0.07−0.08

$\Delta\alpha^{a}$ (arcsec)	$\Delta\delta$ (arcsec)^{a}	P (%)	σ_P	ϕ (deg)	σ_ϕ
−54	−18	2.64	0.88	49.3	9.5
−36	−18	1.76	0.47	60.7	7.8
−36	0	2.54	0.83	54.8	9.0
−36	36	5.82	1.97	46.2	9.6
−18	−54	2.04	0.60	37.4	8.6
−18	−36	1.44	0.27	45.0	5.4
−18	−18	1.18	0.28	48.1	6.8
−18	0	1.65	0.52	47.2	9.0
−18	18	2.16	0.76	57.6	9.2
0	−54	1.17	0.40	176.2	9.9
0	−36	1.13	0.23	4.4	5.8
0	0	0.62	0.22	55.2	9.9
18	−54	1.74	0.46	160.0	7.3
18	−18	0.88	0.23	158.1	7.5
18	54	2.39	0.80	131.4	9.5
36	−36	1.79	0.49	158.1	7.3
36	−18	2.13	0.30	138.7	4.0

[a] Sky positions are relative to $17^{\mathrm{h}}46^{\mathrm{m}}4\overset{\mathrm{s}}{.}3$, $-28^{\circ}54'44\overset{''}{.}3$ (J2000.0).

TABLE 7

M0.11−0.08

$\Delta\alpha^a$ (arcsec)	$\Delta\delta^a$ (arcsec)	P (%)	σ_P	ϕ (deg)	σ_ϕ
−54	18	1.99	0.46	74.9	6.9
−54	36	1.62	0.55	73.2	9.9
−36	−36	1.09	0.35	113.1	9.2
−36	54	2.25	0.51	35.6	6.6
−18	36	1.14	0.29	61.7	7.6
18	−54	2.01	0.60	0.4	8.5
18	−36	0.84	0.22	174.3	7.6
18	−18	1.02	0.19	161.1	5.4
18	0	0.73	0.19	125.8	7.3
36	−36	1.95	0.43	168.1	6.5
36	−18	0.75	0.24	166.3	9.3
36	18	0.93	0.28	151.3	8.9
54	0	1.42	0.46	140.1	9.4

[a] Sky positions are relative to $17^{h}46^{m}10^{s}.2$, $-28^\circ53'6''.3$ (J2000.0).

3. DISCUSSION

3.1. *Morphology of the Inner* 50 pc

The magnetic field vectors inferred from these new data are shown in blue in region III of Figure 1. The black vectors in this region are those from Novak et al. (2000). Also shown in this figure are 100 μm data from the Kuiper Airborne Observatory (Dotson et al. 2000) of the arched filaments (region II) and 60 μm data (Dotson et al. 2000) of the Sickle (region I). The 100 and 60 μm data have beam sizes of 35″ and 22″, respectively. The contours trace 850 μm flux (Pierce-Price et al. 2000). Major molecular features are labeled.

3.1.1. *M−0.13−0.08*

The molecular cloud M−0.13−0.08 (commonly called the 20 km s^{-1} cloud") has an elongated shape, and its long axis is oriented at a shallow (15°) angle to the Galactic plane (see Fig. 1). The cloud is known to be located in front of the Galactic center because it appears in absorption in the mid-infrared (Price et al. 2001). In projection, the long axis of this cloud points in the direction of Sgr A*, a configuration that suggests that this cloud is undergoing a gravitational shear as it falls toward Sgr A*. This is supported by other observations including a high-velocity gradient along the long axis (Zylka, Mezger, & Wink 1990), increasing line widths and temperatures along the cloud in the direction of Sgr A* (Okumura et al. 1991), and an extension of the cloud detected in NH$_3$ emission to within 30″ of Sgr A* in projection (Ho et al. 1991). Novak et al. (2000) have discovered that the magnetic field structure is such that the field is parallel to the long axis of the cloud. They point out that for gravitationally sheared clouds, a consequence of flux-freezing is that regardless of the initial configuration of the field, the field will be forced into a configuration in which it is parallel to the long axis of the cloud. In addition, these authors note that this is not only true for the dense material inside of the cloud but also for the more diffuse molecular material that belongs to the ambient region. Furthermore, they note that the southern end of this cloud exhibits a flare both morphologically and in magnetic field structure. They suggest that this flare is a connection to the large-scale poloidal field traced by the NTFs.

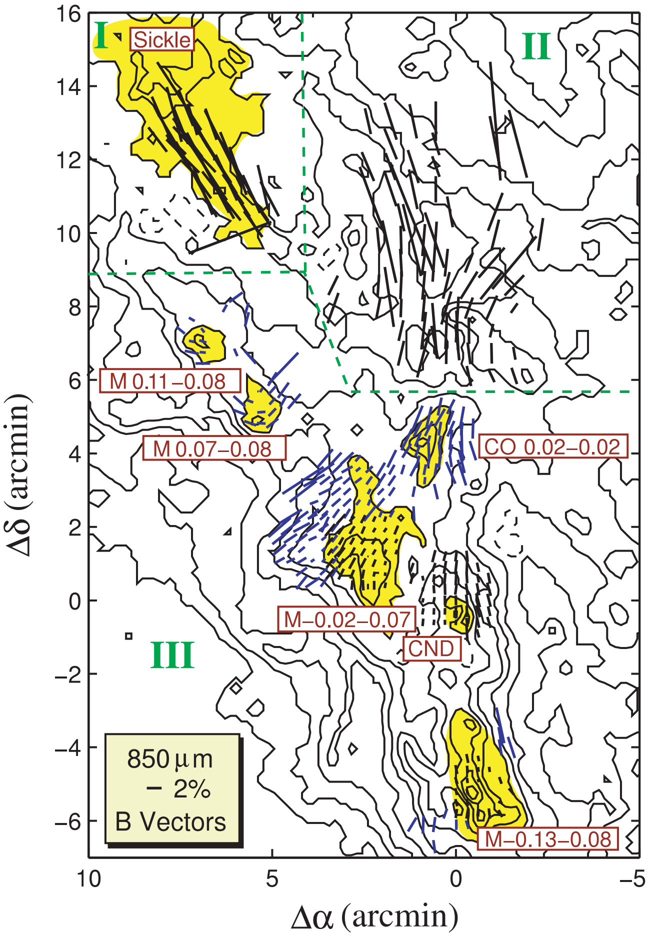

FIG. 1.—Inferred magnetic field directions for polarization measurements in the Galactic center are displayed on 850 μm contours from SCUBA/JCMT (Pierce-Price et al. 2000). The length of each "vector" is proportional to the measured degree of polarization (see key at lower left), and the orientation of each vector is drawn parallel to the inferred magnetic field direction, i.e., perpendicular to the measured direction of polarization. Region I shows 60 μm polarimetery of the Sickle (Dotson et al. 2000). (Note here that the lowermost vector in region I is a bit suspect because of possible reference beam contamination.) Region II shows 100 μm polarimetry of the arched filaments (Dotson et al. 2000). Region III shows new 350 μm polarimetry (*blue vectors*) along with previously published 350 μm polarization results (*black vectors*; Novak et al. 2000). Important dust features are shaded and labeled. The axes scales are offsets in arcminutes from the position of Sgr A* ($\alpha = 17^{h}45^{m}40^{s}.04$, $\delta = -29^\circ00'28''.07$ [J2000.0]). Assuming a distance to the Galactic center of 8.0 kpc, 1′ corresponds to 2.3 pc.

Our seven new vectors in this region provide additional support for this interpretation, but a more extensive polarimetric mapping of this cloud is necessary before a complete interpretation is made.

3.1.2. *G0.18−0.04*

The H II region G0.18−0.04 (commonly called the Sickle) can be seen in 20 cm thermal emission in Figure 2. It is believed to be the ionized surface of a molecular cloud that is interacting with the radio arc (Serabyn & Güsten 1991). Its molecular counterpart (M0.20−0.033; Serabyn & Morris 1994) can be seen in Figure 3*b*. It has been suggested that this interaction is responsible for producing the relativistic electrons necessary to light up the radio arc via magnetic reconnection (Serabyn & Güsten 1991; Davidson 1996).

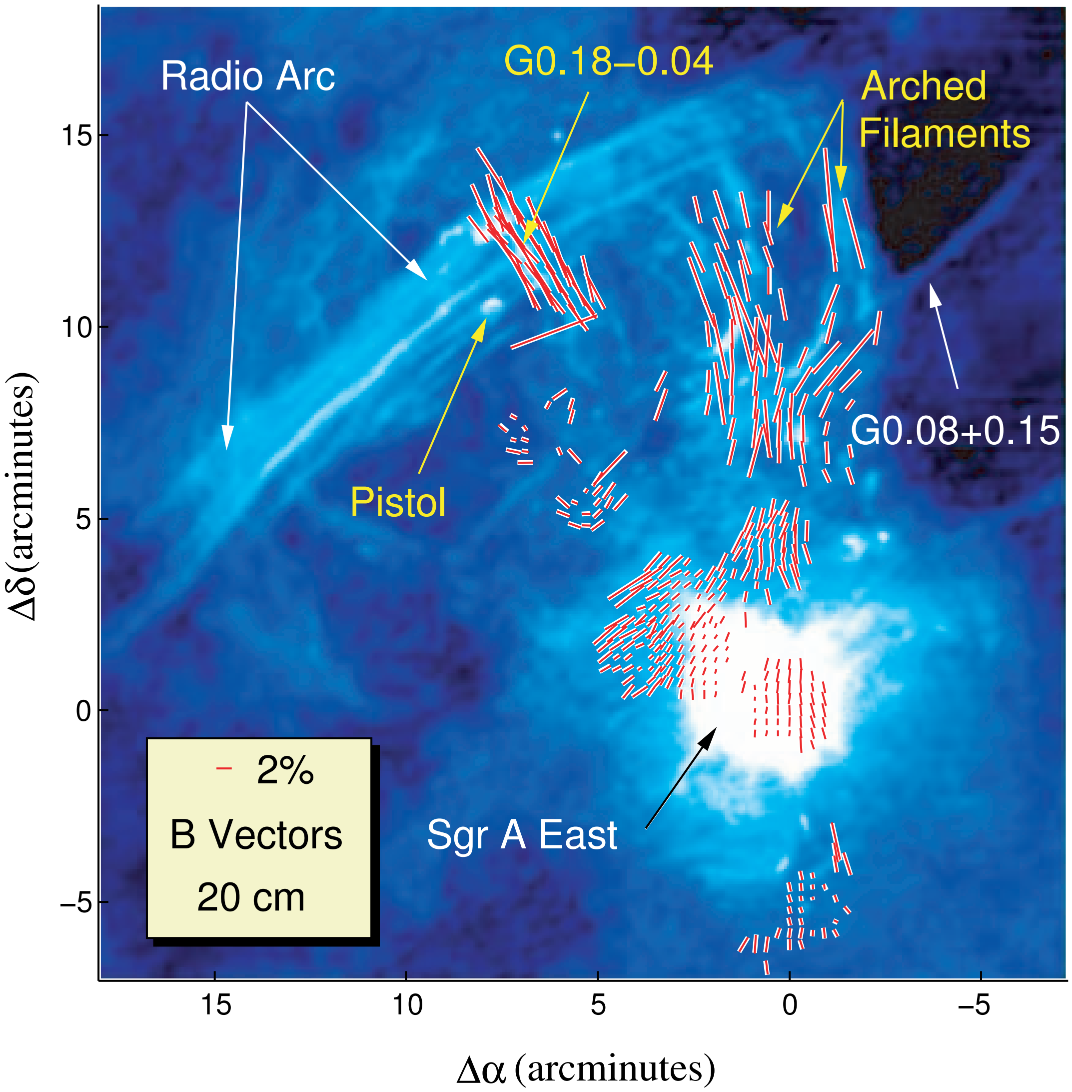

FIG. 2.—Inferred *B*-vectors superposed on a 20 cm continuum VLA image (Yusef-Zadeh et al. 1984). Important thermal and nonthermal structures are labeled in yellow and white, respectively. The 100 μm vectors appear to trace the arched filaments. The magnetic field in the molecular cloud associated with G0.18−0.04 (the Sickle) is perpendicular to the field traced by the NTFs of the radio arc.

The relationship between the geometry of the cloud and its magnetic field structure is similar to that of M−0.13−0.08. The cloud is elongated parallel to the plane of the Galaxy, and its magnetic field, as inferred from far-infrared polarimetry, is parallel to the long axis. These similarities to M−0.13−0.08 suggest a similar origin of the field geometries of the two clouds.

One difference between this cloud and M−0.13−0.08 is that in the case of the former there is no observed flaring of the field. This fact makes it difficult to determine the direction of the motion in the plane of the sky. The stark 90° difference between the toroidal field observed in the molecular material and the pristine poloidal geometry of the superposed radio arc manifests little morphological connection between the toroidal field and the poloidal field in this vicinity. There are several possibilities for why this might be the case. First, the polarimetry coverage may be too limited in this region. More data taken in surrounding region may reveal a connection to a poloidal field. Second, this cloud may be more evolved than M−0.13−0.08, and so we may be observing a magnetic field that has had enough time to shear into a more parallel configuration than that of M−0.13−0.08. Finally, because this molecular cloud is farther from the dynamical center of the Galaxy than M−0.13−0.08, the tidal forces on it are weaker, thus allowing for a more uniform shearing along its length.

3.1.3. *M0.11−0.08 and M0.07−0.08*

M0.11−0.08 and M0.07−0.08 are two peaks of a molecular cloud complex that, like M−0.13−0.08 and the molecular cloud associated with the Sickle, is elongated nearly parallel to the plane with its long axis directed toward Sgr A*. The radial velocity of this complex has been measured to be ~50 km s^{-1} (see Fig. 3*c*).

The inferred magnetic field configuration for this complex displays a geometry that is quite unique. The field appears to tightly wrap around the southern and eastern edges of this cloud. One possible interpretation of the curvature of the magnetic field is that the cloud is moving toward the

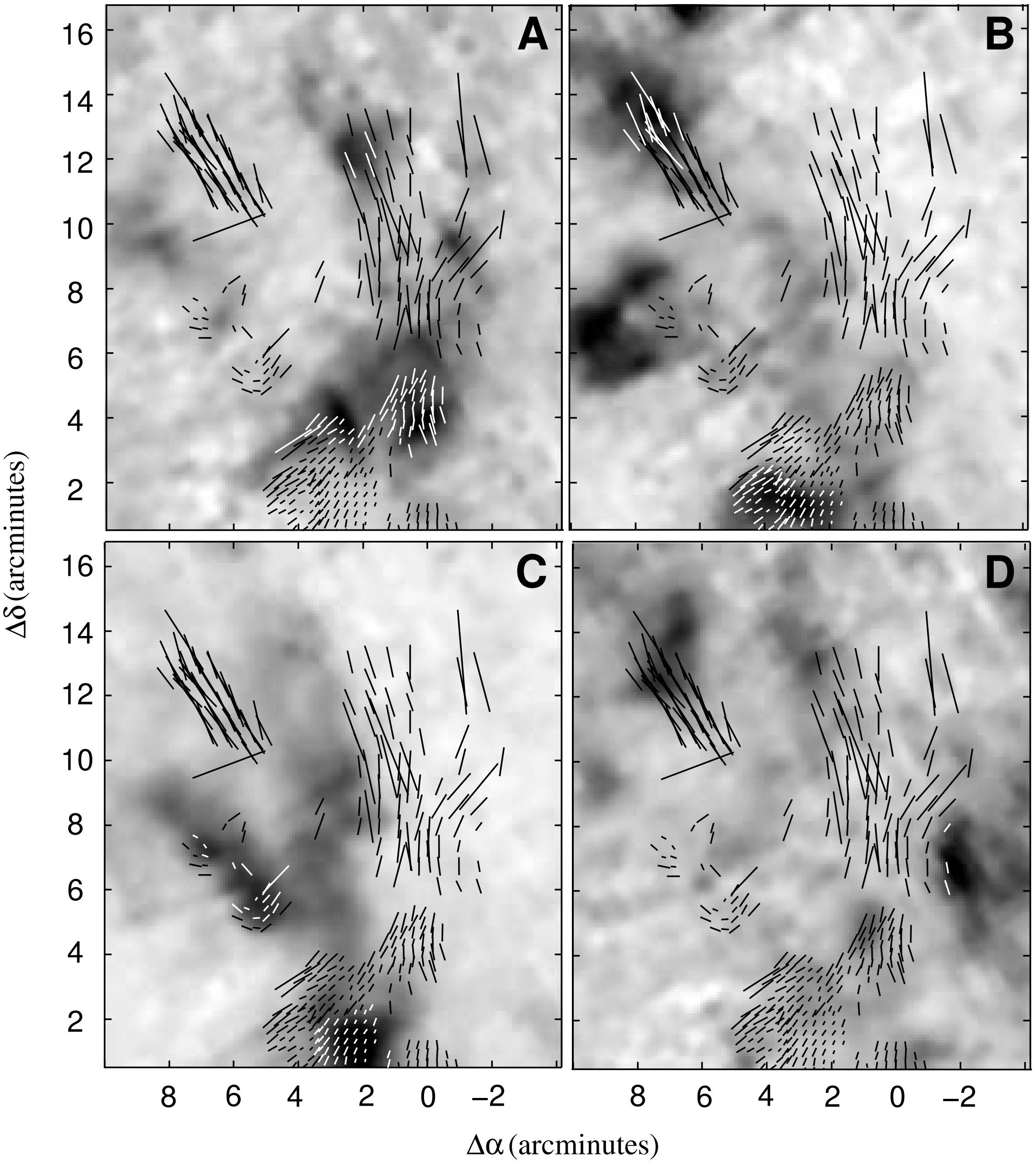

FIG. 3.—Maps of CS line emission (Tsuboi, Ukita, & Handa 1997) with polarization data superposed. The origin of the coordinate system is Sgr A*. (*a*) Structures at ~ -15 km s^{-1}, the most prominent of which is the molecular material associated with the arched filaments. (*b*) Material at ~ 30 km s^{-1}. The molecular material associated with the Sickle ($v \sim 25$ km s^{-1}) is visible here. (*c*) Material at ~ 50 km s^{-1}. M−0.11−0.08, M0.07−0.08, and M−0.02−0.07 are all prominent at this velocity. Note that the magnetic field vectors at the southwestern edge of M0.07−0.08 trace the edge of the cloud. This suggests that the cloud has a velocity in the plane of the sky that is directed toward M−0.02−0.07, a region of predominantly poloidal flux. (*d*) Material at ~ 85 km s^{-1}. Note the edge of the bright cloud in the lower right of the panel seems to be traced by the 100 μm magnetic field vectors.

Sgr A* region in projection and is sweeping up magnetic flux from the intercloud medium. The direction of travel inferred from the polarization data indicates that in projection, this cloud is moving toward a region dominated by a poloidal field (see northeast side of M−0.02−0.07 in Fig. 1). As the cloud moves through the less dense intercloud medium, this poloidal flux then is wrapped around the cloud into a toroidal configuration as seen along the eastern edge of the cloud. The result is an observed transition between poloidal and toroidal fields.

In the densest regions of this cloud complex, there are few measurements; however, those that exist hint at a field that is parallel to its long axis, similar to that of M−0.13−0.08 and the molecular cloud associated with the Sickle.

3.1.4. *The* X *Polarization Feature*

The 350 μm polarimetric observations of M−0.02−0.07, the circumnuclear disk (CND), and CO 0.02−0.02 provide evidence for a magnetic field structure that is continuous with that derived from the 100 μm polarimetric observations of the arched filaments to form an "X-shaped" feature that we will refer to as the "X polarization feature." The feature extends (in the coordinate system of Fig. 1) from (−1′, 13′) down through (5′, 0′). This feature is centered on CO 0.02−0.02. Its upper arms are traced by the arched filaments, and its lower arms end in M−0.02−0.07 and M−0.13−0.08. The organization of the magnetic field vectors appears to be on scales (50 pc) significantly larger than those of typical Galactic center molecular clouds (5–10 pc). This fact reinforces the notion that the vectors trace a single global field that is subject to environmental forces. The continuity of the vectors on the eastern side of this feature suggest that these vectors may trace the edge of an expanding shell.

Another possibility is that the X polarization feature is a line-of-sight superposition of regions of poloidal and toroidal fields. The orientation of the observed magnetic field at any given location depends on the relative polarized emission from poloidal and toroidal regions that intersect the line of sight. For example, the poloidal field is seen to dominate in the eastern part of the M−0.02−0.07 cloud and at the western edge of the arched filaments. The toroidal field dominates at the eastern edge of the arched filaments and around the CND. The two fields mix in CO 0.02−0.02.

Another example of line-of-sight mixing of poloidal and toroidal fields occurs at the western edge of the arched filaments. Here there exist several magnetic field vectors oriented perpendicular to the plane that are in close proximity to G0.08+0.15 (see Fig. 2), an NTF that traces the poloidal field. Just to the north, the magnetic field vectors return quite abruptly to a toroidal configuration in the vicinity of the molecular features that correspond to the arched filaments. It is possible that the molecular material at $v \sim -15$ km s^{-1} (See Fig. 3*a*) is displaced along the line of sight from G0.08+0.15 and that the net polarization observed consists of contributions from dust associated with the respective neighborhoods of these two features. To the south of G0.08+0.15, the vectors again become indicative of a field distorted by gravity as they wrap around the molecular cloud visible in Figure 3*d*.

3.2. *Polarized Flux*

Figure 4 shows the relationship between Galactic center polarization magnitude measured by Hertz and the 350 μm flux measured by the Submillimeter High Angular Resolution Camera (SHARC), a 350 μm photometer with a 15″ beam (Dowell et al. 1999). A linear fit to this log-log plot gives a slope of −0.67. In this plot, we have included all points with a polarization signal-to-noise ratio (S/N) greater than 3 and have corrected the polarization by $P' = (P^2 - \sigma_P^2)^{1/2}$ in order to account for the systematic overestimation of polarization (Serkowski 1974) inherent in the conversion from q and u to P and ϕ. Figure 4 shows a depolarization effect associated with an increase in 350 μm flux.

Because of a concern over a selection effect that systematically excludes low polarizations at low fluxes, the test was repeated with an S/N cutoff of 1. In this case, the resulting slope is −0.73, which is not very different from −0.67. We conclude that this selection effect is of minimal importance. The test was repeated for the 11 individual Hertz pointings corresponding to both this work and that of Novak et al. (2000). For each pointing, a polarization versus flux comparison was made using measured relative fluxes that we obtained simultaneously with the polarization measurements. In this way, for each pointing, we obtained a slope. The average of these slopes was −0.96, and the standard deviation was 0.32.

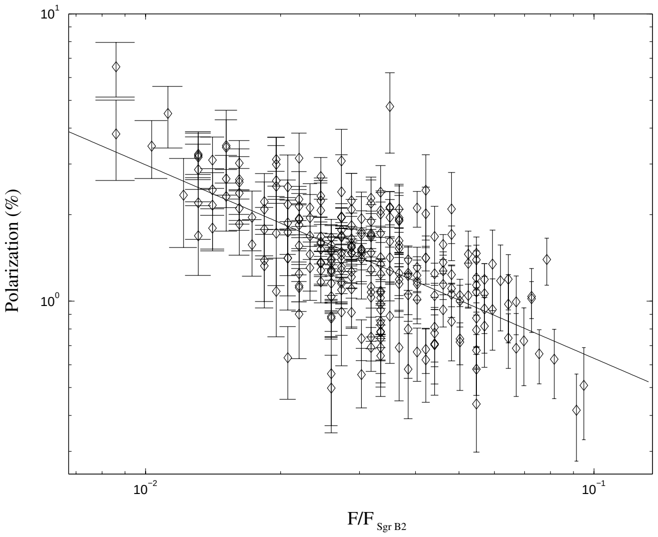

FIG. 4.—The 350 μm polarization plotted against 350 μm flux. The polarization data are from Novak et al. (2000) and this work, with a 3 σ cutoff applied. The flux values are from SHARC/CSO (Dowell et al. 1999) and are expressed as a fraction of the flux measured at the peak of Sgr B2. The slope of the best-fit line is −0.67.

These slope values are similar to those found by Matthews, Wilson, & Feige (2001) and Matthews et al. (2002) for various Galactic molecular clouds. Matthews et al. (2002) suggest three possibilities for the depolarization effect (see also Schleuning 1998 and Dotson 1996). First, the lower polarization could be due to poor grain alignment or low polarization efficiency in the cores of these clouds. Second, the depolarization could be a result of a geometrical cancellation of the front and back of a three-dimensional field that is threaded through the optically thin cloud. Finally, it is possible that turbulence in the cores of clouds leads to a spatial structure of the magnetic fields that is too small to be resolved by Hertz's beam.

The evidence for depolarization in the Galactic center does not provide enough information to differentiate among the three proposed explanations; however, it does indicate that the depolarization effect is observable in regions that are a factor of ∼10 larger than molecular clouds in the disk of the Galaxy.

3.3. *Polarization Angle versus Flux*

Figure 5 illustrates the dependence of the polarization angle on the flux measured by SHARC (Dowell et al. 1999). In this figure, the absolute deviation from a poloidal field ($|\phi - \phi_{\rm poloidal}|$) is plotted against 350 μm flux. At high fluxes we find the field to be generally toroidal, while at low fluxes, the field tends to be more poloidal in direction. In the following discussion, we offer two explanations for this relationship.

One possible interpretation of this result relies again on the model of Uchida et al. (1985). In this picture, the field in the neutral clouds was initially in a poloidal configuration. In regions where the gravitational energy density is higher than the energy density due to the magnetic field, the motion of the dense clouds has sheared the field into a toroidal configuration. Put another way, the underdense regions are dominated by magnetic energy, and thus the initial poloidal

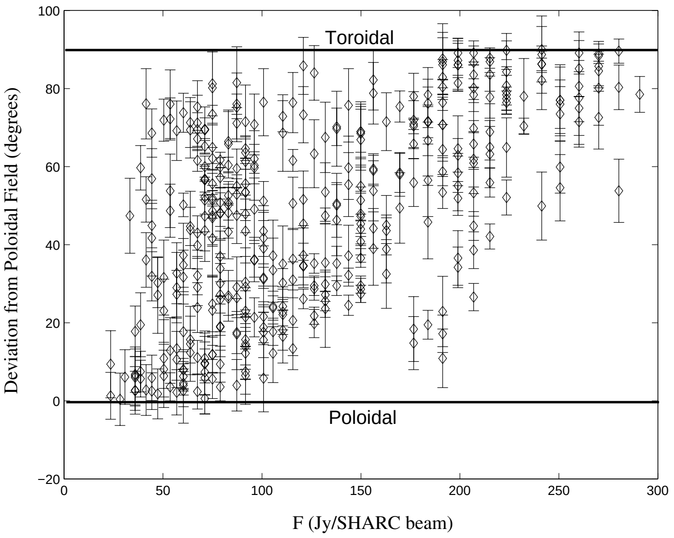

FIG. 5.—For each of the polarization measurements in Fig. 1, we plot the magnitude of the difference between the magnetic field direction and the perpendicular to the Galactic plane versus 350 μm flux. The 350 μm flux was measured by SHARC/CSO (Dowell et al. 1999) using a 15″ beam. By including polarization measurements for all three wavelengths, we are assuming that the polarization angle will not change significantly from 60 to 350 μm.

field configuration is preserved. Conversely, in overdense regions, the magnetic energy density is insufficient to overcome the kinetic motions of the clouds in the Galactic potential, and thus the field is observed to be toroidal.

Assuming that this model applies to the relationship manifested in Figure 5 allows one to estimate a characteristic strength for the magnetic field that threads the neutral clouds in the central 50 pc. One can infer that there exists a critical mass density at which the energy density of the poloidal field equals that of the gravitational energy density. In order to proceed with the estimate, we will assume that this density corresponds to a measured angle $|\phi - \phi_{\rm poloidal}| = 45°$. This choice is somewhat arbitrary. In order to find the flux corresponding to this angle, we perform various binnings as shown in Figure 6. Linear fits to each of these four plots give a flux of 125 Jy beam^{-1}. To a crude approximation, this energy balance condition is represented by

$$\frac{1}{2}\rho v^2 = \frac{B^2}{8\pi} . \quad (1)$$

Here the kinetic energy density of material orbiting in the gravitational potential well of the Galaxy is equated to the magnetic energy density.

The key to this problem now becomes the estimate of ρ and v. The velocity, v, can be estimated from typical cloud velocities (Tsuboi, Handa, & Uchida 1999) and is expected to be 50–150 km s^{-1}. The density can be determined as follows.

The brightness one observes from a thermal source having an optical depth τ_ν is

$$I_\nu = B_\nu(T)(1 - e^{-\tau_\nu}) , \quad (2)$$

where $B_\nu(T)$ is the Planck function.

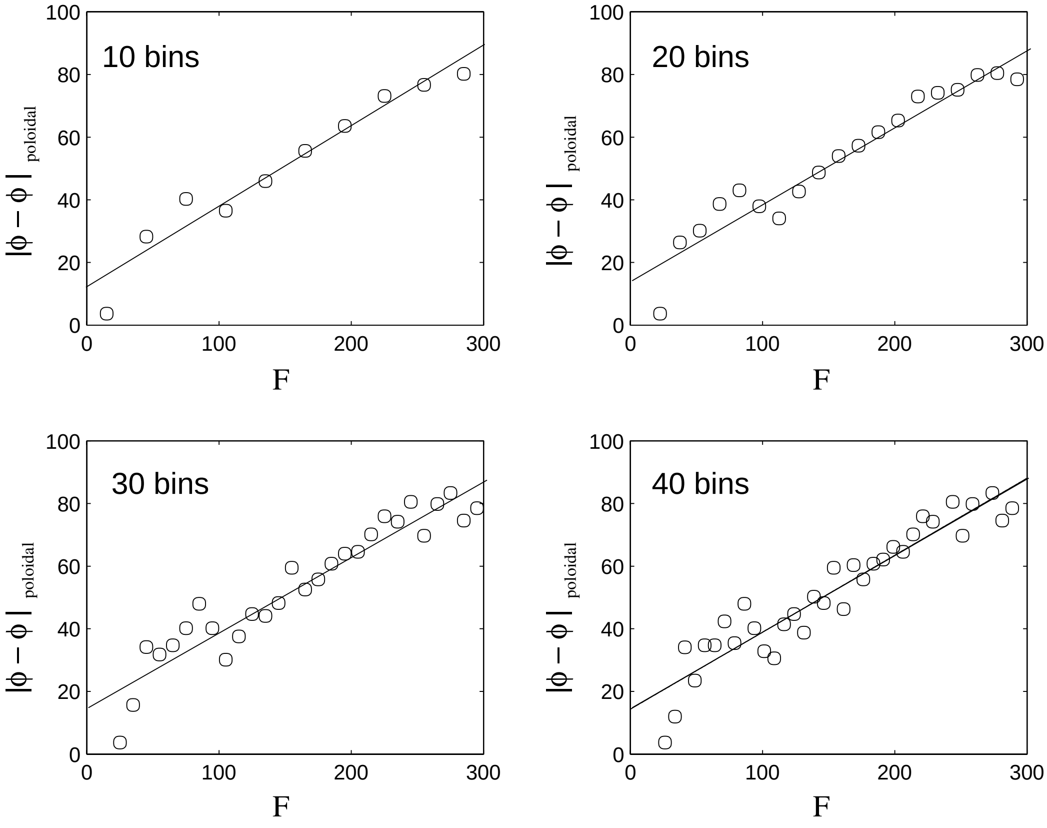

FIG. 6.—The points in Fig. 5 are grouped into flux bins, and the mean polarization angle in each bin is plotted against the mean flux in each bin. For each binning, the critical flux for equality of magnetic and gravitational forces has been calculated by fitting a line and then determining the flux value for a 45° deviation from a poloidal field. The average of the four resulting values for the critical flux is 125 Jy beam^{-1}, and the standard deviation is ~ 1 Jy beam^{-1}.

In the case of 350 μm observations, the optical depth is generally small. For $\tau_\nu \ll 1$,

$$I_\nu = \tau_\nu B_\nu(T)\ . \qquad (3)$$

SHARC measures $F_\nu = I_\nu \Delta\Omega$, the flux of the incoming radiation, where $\Delta\Omega$ is the solid angle subtended by a SHARC array element. From these equations, it is possible to express the optical depth of the dust layer as a function of temperature and measured flux:

$$\tau_\nu = \frac{F_\nu}{B_\nu(T)\Delta\Omega}\ . \qquad (4)$$

We can also express the optical depth as a function of grain properties along the line of sight. Once again, we are working in the limit $\tau_\nu \ll 1$. We can imagine a column of dust along the line of sight that extends through the entire depth of the Galactic center. The optical depth is proportional to the number density of dust grains along the line of sight (N_d). It is also proportional to the typical geometrical cross section of each of the grains (σ_d); however, since the grain sizes are generally much smaller than the wavelength of the radiation, the efficiencies of the grains for emitting, scattering, or absorbing light are much lower than this blackbody approximation indicates. Thus, we write the optical depth as

$$\tau_\nu = N_d Q_e \sigma_d\ , \qquad (5)$$

where Q_e is the emissivity of the dust grains and is generally much less than unity for submillimeter radiation.

Once the N_d is found, the total dust mass observed by a SHARC beam is

$$M_d = N_d \rho_d v_d \Delta\Omega D^2\ . \qquad (6)$$

Here D is the distance to the source and $\Delta\Omega D^2$ is simply the physical size of SHARC's beam at a distance D; ρ_d and $v_d \sim (4/3)\pi a^3$ are the density and volume of a dust grain, respectively. If we then make the appropriate substitutions and assume a gas-to-dust ratio, $X \gg 1$, we get the following expression for the total mass:

$$M = \frac{4F_\nu \rho_d a D^2 X}{3Q_e B_\nu(T)}\ . \qquad (7)$$

Putting in the appropriate numbers for 350 μm radiation yields

$$\frac{M}{M_\odot} = \frac{F_\nu}{\text{Jy}}\, \frac{\rho_d}{\text{g cm}^{-3}}\, \frac{a}{\mu\text{m}} \left(\frac{D}{\text{kpc}}\right)^2 \frac{X}{Q_e}\, 6.9 \times 10^{-7}(e^{41.1/T} - 1)\ . \qquad (8)$$

The density can be calculated by assuming a value for the depth of the dust layer (L):

$$\rho = \frac{M}{\Delta\Omega D^2 L}\ . \qquad (9)$$

We use the grain properties of Dowell et al. (1999; see also Hildebrand 1983) for our grain model. These are $a = 0.1$ μm, $Q_e = 1.9 \times 10^{-4}$, $X = 100$, and $\rho_d = 3$ g cm^{-3}. In addition, Pierce-Price et al. (2000) have used the Submillimeter Common-User Bolometric Array (SCUBA) on the James Clerk Maxwell Telescope (JCMT) to map the CMZ at 450 and 850 μm. They have found the dust temperature to be relatively uniform over the CMZ and adopt a value of 20 K. With these numbers, one can get an estimate of the magnetic field strength as a function of velocity of the material and the thickness of the dust layer:

$$B = 3\ \text{mG}\left(\frac{L}{200\ \text{pc}}\right)^{-1/2} \frac{v}{100\ \text{km s}^{-1}}\ . \qquad (10)$$

Based on CS measurements of the CMZ (Tsuboi et al. 1999), most molecular material has $v < 150$ km s^{-1}. The CMZ has a projected diameter of 200 pc (Morris & Serabyn 1996). Assuming cylindrical symmetry, this is approximately the depth of the material along the line of sight.

The magnetic field configuration is most certainly more complicated than in the simple model assumed here. Specifically, the field strength is most likely not constant over the regions of different field geometries. In addition, our estimates of the various parameters that enter into the calculation contain uncertainties and will most likely be refined with additional measurements. However, the crux of the above calculation is that if this model is correct, the submillimeter and far-infrared polarimetric observations are consistent with a mG field that permeates the cold dust of the central 50 pc.

Based on ram pressure equilibrium arguments, Yusef-Zadeh & Morris (1987a, 1987b)have argued that the field in the radio arc is $\sim$1 mG. Furthermore, it has been suggested (Yusef-Zadeh & Morris 1987a, 1987b) that a uniform poloidal field permeates the central 50 pc. However, the theory of a pervasive mG field has several potentially serious problems. Most notably, a 3 mG field yields a synchrotron lifetime of a few hundred years. Such a short lifetime makes it difficult to explain the synchrotron features in the Galactic center. Even if one assumes that the above calculation is slightly overestimated and that the field is of the order 1 mG, the synchrotron lifetime estimate is still only a few thousand years. In order to get around such an objection, one could postulate the existence of many sources of relativistic electrons scattered throughout the central 50 pc; however, there is little direct evidence for this.

In addition, with the exception of localized OH maser emission studies (Yusef-Zadeh et al. 1996) and studies of the CND (Plante, Lo, & Crutcher1995), there is little evidence for such strong fields from direct Zeeman measurements. Sofue et al. (1987) have derived fields of 10–100 μG for the arched filaments and the radio arc using Faraday rotation measurements. Using equipartition arguments, Tsuboi et al. (1986) have found a field of the same order in the plumes that make up the extension of the radio arc on the eastern side of the Galactic center lobe. More recently, Uchida & Güsten (1995) have used a large beam to probe eleven fields in the CMZ and were unable to detect such strong fields.

On the other hand, the line-of-sight field probed by both Zeeman and Faraday rotation measurements may be naturally suppressed by the intrinsic field geometries. In the central 50 pc, the above model would predict geometries that are mostly confined to the plane of the sky. In the case of Uchida & Güsten (1995) the beam sizes may be large enough such that spatial variations of the field within the beam may be causing the strength of the field to be underestimated.

In the wake of the above caveats, we cautiously associate the field in the underdense neutral regions with that observed in the hot gas. In this case, the global poloidal field postulated by Yusef-Zadeh & Morris (1987a, 1987b) couples to the neutral clouds and becomes sheared into a toroidal field in regions of gravitational dominance.

Because of the problems with the pervasive mG field hypothesis, we propose an alternative explanation for the relationship seen in Figure 5. Conceivably, winds due to supernovae in the Galactic center could result in driving an initially toroidal field into a vertical configuration. Recently, Bland-Hawthorn & Cohen (2003) have found mid-infrared features that they have interpreted as a bipolar wind having an energy on the order of 10^{55} ergs. Such an energy is comparable to that of a ~mG field in the region of interest and could be responsible for the relationship seen in Figure 5.

The idea that winds are responsible for the pattern seen in the polarimetric observations also has problems. The geometry of the radio arc makes it difficult to explain this feature using a bipolar wind. Thus, it seems likely that there is a poloidal field in the Galactic center, and it is logical that the vertical fields we find in the underdense neutral regions be associated with this poloidal field. In addition, the polarimetry data for clouds such as M−0.13−0.08, M0.11−0.08, and M0.07−0.08 suggest a transition to a toroidal geometry rather than from a toroidal geometry. Higher resolution polarimetry combined with increased spatial coverage may be able to differentiate between these two possible processes.

3.4. *Reference Beam Contamination*

In performing differential measurements using chopping techniques, polarized flux in the reference beam positions is always a potential hazard. Because of the extended nature of the dust in the Galactic center, it is of particular importance to understand the possible effect of reference beam contamination on the data presented here. Several attempts have been made to quantify this issue (Novak et al. 1997; Schleuning et al. 1997; Matthews et al. 2001). The goal of this section is to assess the level of reference beam contamination in our data. Note that throughout this analysis quantities pertaining to the "reference beam" such as P_r and I_r refer to the average of these quantities over the multiple reference beam positions used in the observations.

Since the quantitative result of this work centers on the relationship shown in Figure 5, we are concerned primarily with the polarization angle (ϕ), and so we wish to estimate the maximum effect of polarized flux in the reference beam on ϕ. For the rest of this section, we follow the notation of Novak et al. (1997), who give the difference between the source polarization angle (Φ_s) and that measured (Φ_m) as

$$\Phi_s - \Phi_m = \frac{1}{2}\tan^{-1}\left(\frac{P_r w \sin 2\delta}{\sqrt{P_m^2 - P_r^2 w^2 \cos 2\delta}}\right) . \qquad (11)$$

Here P_r is the polarization in the reference beam, δ is the difference between the measured polarization angle and the polarization angle of the reference beam ($\Phi_m - \Phi_r$), and w is the ratio of flux in the reference beam to that measured for a given source (I_r/I_m). Alternatively, since $I_s = I_m + I_r$, w can be expressed as $(I_s/I_r - 1)^{-1}$. Here I_s is the intrinsic source flux.

It is desirable to estimate the maximum effect the reference beam contamination could have on these measurements. Specifically, we wish to understand how reference beam contamination could affect the results shown in Figures 5 and 6.

In order to evaluate equation (11), we need to make estimates of w, P_m, P_r, and Φ_r. We find from the SCUBA survey (Pierce-Price et al. 2000) that the average ratio of the flux in the main beams of our six sources to that in the reference beams is $I_s/I_r = 1.9$. This leads to $w = 1.1$. The average 350 μm polarization measured by Hertz in the Galactic center is 1.9%. Thus, we assign $P_m = 0.019$.

Finally, we need to make an estimate of P_r and Φ_r, the quantities describing the polarization properties of the reference beam flux. To do this, we note that Novak et al. (2003) have mapped the CMZ in 450 μm polarimetry. They find that the average polarization into a 5′ beam is 1.4% and that the field is nearly toroidal. Because they use a 30′ chop throw, their reference beam is well off of the CMZ, and the contamination should be negligible. Assuming no significant wavelength dependence between 350 and 450 μm, we set $P_r = 0.014$ and $\Phi_r = -58\overset{\circ}{.}4$, the polarization angle that corresponds to a toroidal field.

The difference between the measured and actual polarization angle ($\Phi_s - \Phi_m$) under the above assumptions is plotted versus measured polarization angle (Φ_m) in Figure 7. The maximum error is ±20°. Note that the amplitude of this error is independent of the chosen value of Φ_r since the curve simply shows the error in the measured polarization angle as a function of the difference between the measured polarization angle and the reference beam polarization angle. (In this case, we have set the reference beam polarization angle to an "arbitrary" value.) The potential error induced by reference beam contamination is systematically about twice that of our maximum allowable statistical error. (An S/N of 3 implies $\sigma_\phi \sim 10°$.) Although this is potentially large, it is not large enough to cause poloidal fields to be measured as toroidal and vice-versa. Therefore, it is unlikely that the relationship shown in Figures 5 and 6 is caused by reference beam contamination.

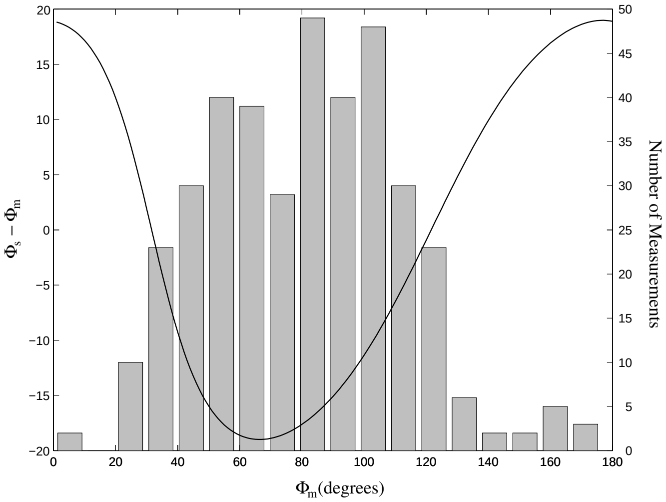

FIG. 7.—The solid curve shows the predicted difference between the intrinsic source polarization angle and the measured polarization angle plotted as a function of measured polarization angle. The effect is due to the polarized flux in the reference beam. The assumptions involved in this prediction are discussed in § 3.4. Also shown is the distribution of measured angles of polarization for the new 350 μm polarization data presented in this paper.

We can quantitatively estimate the potential effect of reference beam contamination on our results. This histogram in Figure 7 shows the number of measurements having a polarization angle in each of the 10° bins. As an unfortunate coincidence, the error is not symmetric with respect to our data, and thus it is expected that there will be a bias in our field strength estimate. We have applied this correction to the data and the resulting ϕ versus F plot has the same basic appearance; however, the equilibrium point once the correction is applied is 168 ± 2 Jy (SHARC beam)$^{-1}$. This implies at most a 30% error in our magnetic field strength estimate.

It must be noted that because the large-scale field in the Galactic center has been found to be toroidal by Novak et al. (2003), it is possible that a significant amount of dust is present along the line of sight to the central 50 pc that is permeated by this toroidal field and will emit polarized radiation accordingly. The large-scale contribution to the polarized flux can be modeled by a uniform sheet of polarized flux. In this case, chopping can be an advantage in observing magnetic fields in the central 50 pc since it removes the contribution from a uniform field in the foreground and background dust. This model may also explain the lack of polarization measurements by Novak et al. (2003) in the central 50 pc in regions where Hertz sees a poloidal field. Because of its 6′chop, Hertz may be sampling a smaller volume along the line of sight than that sampled by Novak et al. (2003). In the latter case, line-of-sight superposition of the uniform sheet and the polarized emission detected by Hertz may cancel, resulting in unpolarized radiation.

3.5. *NTF Generation*

It has been discovered that many of the NTFs in the Galactic center are associated with molecular clouds (Serabyn & Güsten 1991; Staguhn et al. 1998). This has led to the suggestion that the acceleration mechanism for the relativistic electrons in the NTFs is magnetic reconnection (Serabyn & Morris 1994). The magnetic reconnection is believed to be precipitated by the collision of the cloud with a magnetic flux tube by either distorting the fields in the flux tube or forcing these fields into contact with those in the cloud.

The notion that the poloidal and toroidal fields have the same origin suggests a third option for the magnetic reconnection scenario. Figure 8 illustrates this idea.

In the Galactic center, relatively diffuse molecular gas is supported by magnetic pressure (Fig. 8*a*); however, this material is free to collapse along the field lines. As the gas collapses, gravitational energy becomes increasingly important. Gravity can accelerate the cloud, and the resulting differential motion between the material in the cloud and that of the ambient medium can begin to shear the magnetic field (Fig. 8*b*). This shear continues until the field is more toroidal than poloidal (Fig. 8*c*). Note that the field external to the clouds is still quite poloidal because magnetic energy dominates the dynamics of this region. Finally, if the gravitational energy is large enough, and the system is given the time to evolve, the oppositely oriented fields in the center of the cloud may be squeezed together to enable reconnection. This process releases energy that can produce the relativistic electrons required to " light up " the filaments.

Submillimeter and far-infrared polarimetry in concert with radio and submillimeter photometric observations present a picture of molecular material at the various evolutionary stages shown in Figure 8. From the polarimetry data in Figure 1, we can see examples of each of the four panels in Figure 8. The area to the north and east of M−0.02−0.07 is an example of the situation depicted in Figure 8*a*. Here the molecular material is not very dense, and the magnetic field is perpendicular to the Galactic plane. An example of Figure 8*b* is the molecular cloud complex containing M0.07−0.08 and M0.11−0.08. Here the field is seen to be shearing around the front edge of M0.07−0.08, making a transition from poloidal to toroidal at the southern edge of the cloud. The 20 km s^{-1} cloud (M−0.13−0.08) is thought to be shearing out its magnetic field as it falls toward Sgr A* (Novak et al. 2000). The flare seen at the southern end may indicate that it has not yet reached the point where magnetic reconnection is occurring and hence best matches Figure 8*c*.

The interaction of the Sickle with the GCRA gives the best example of Figure 8*d*. Here the magnetic field in the molecular cloud is observed to be nearly perfectly aligned with the direction of both the long axis of the cloud and the Galactic plane. Filaments, namely, those of the GCRA, are observed and appear to diffuse into G0.18−0.04, the H II region associated with this interaction. Here depolarization of the filaments is observed (Lesch & Reich 1992). The clumpiness of the H II region and the structure of the filaments themselves may stem from the irregularities of the interior of the cloud where reconnection takes place.

It is possible that there are similar occurrences in places such as the arched filaments where there is also an observed transition from toroidal to poloidal fields adjacent to an NTF (in this case, the northern thread). In order to test this idea with respect to other filaments and clouds in the Galactic center, more complete polarimetric coverage of the central 50 pc is required.

4. SUMMARY

We have presented new submillimeter polarization measurements in the CMZ of our Galaxy and have found that the measurements in overdense regions are indicative of a toroidal magnetic field structure, while those in underdense regions suggest a poloidal configuration. We have offered two explanations and tentatively favor the scenario in which the dense material shears out an initially poloidal field rather than the alternative scenario in which winds are responsible for deforming a toroidal field. However, our knowledge of the Galactic center magnetosphere is far from complete, and more data are necessary before we can definitively decide between these two models.

The authors would like to thank Farhad Yusef-Zadeh, S. Harvey Moseley, and Johannes Staguhn for their helpful insights. Funding for this work was provided by NSF grants AST-9987441 and -0204886 to R. H. H., NSF CAREER Award OPP-9618319 to G. N., NASA GSRP award NGT 5-88 to D. T. C., and an NRC Posdoctoral Associateship to D. T. C. The CSO is funded by NSF grant AST-0229008.

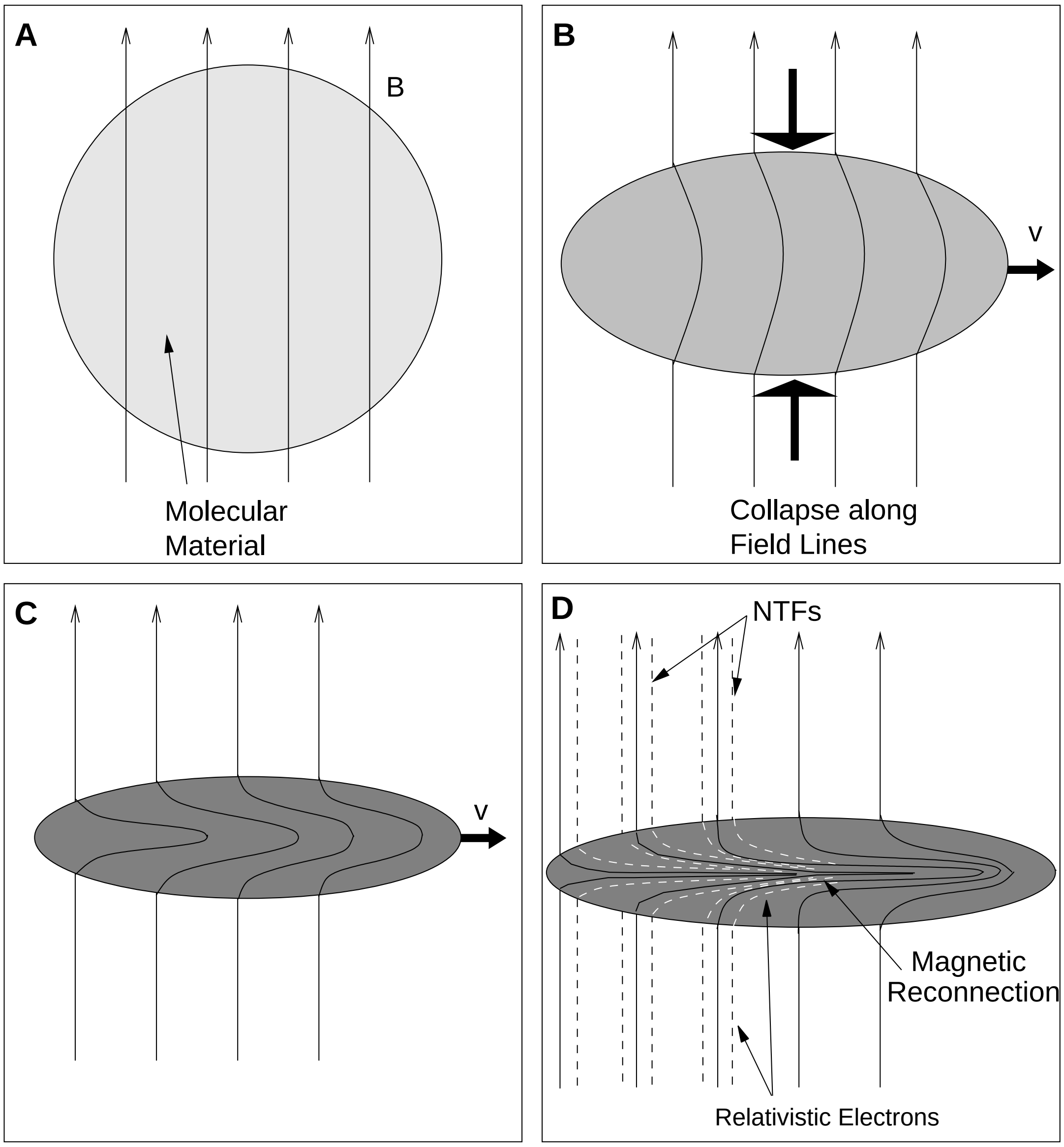

FIG. 8.—Molecular clouds can produce relativistic electrons necessary for the illumination of NTFs by the following process. In regions of low density, the molecular material is dominated by the magnetic field, and we observe a poloidal field (panel *a*). Cloud material is free to move along lines of magnetic flux. In this way, the material can form clouds where the gravitational energy density grows to values comparable to the magnetic field energy density. At this stage, velocities of the molecular material with respect to the poloidal field can distort the field (panel *b*). Shearing motion will then be able to distort the field. The process continues (panel *c*) until the field inside the cloud is predominantly toroidal. Finally, oppositely oriented magnetic fields near the cloud centers will be forced into contact by shearing and will reconnect, thereby releasing energy that energizes relativistic electrons. These electrons spiral along the external field and produce synchrotron radiation that we observe as an NTF (panel *d*).

REFERENCES

Bland-Hawthorn, J., & Cohen, M. 2003, ApJ, 582, 246
Davidson, J. A. 1996, in ASP Conf. Ser.97, Polarimetry of the Interstellar Medium, ed. W. G. Roberge & D. C. B. Whittet (San Francisco: ASP), 504
Dotson, J. D., Davidson, J., Dowell, C. D., Schleuning, D. A., & Hildebrand, R. H. 2000, ApJS, 128, 335
Dotson, J. L. 1996, ApJ, 470, 566
Dowell, C. D., Hildebrand, R. H., Schleuning, D. A., Vaillancourt, J. E., Dotson, J. L., Novak, G., Renbarger, T., & Houde, M. 1998, ApJ, 504, 588
Dowell, C. D., Lis, D. C., Serabyn, E., Gardner, M., Kovacs, A., & Yamashita, S. 1999, in ASP Conf. Ser. 186, The Central Parsecs of the Galaxy, ed. H. Falcke, A. Cotera, W. Duschl, F. Melia, & M. Rieke (San Francisco: ASP), 453
Hildebrand, R. H. 1983, QJRAS, 24, 267
Ho, P. T. P., Ho, L. C., Szczepanski, J. C., Jackson, J. M., & Armstrong, J. T. 1991, Nature, 350, 309
LaRosa, T. N., Kassim, N. E., Lazio, T. J. W., & Hyman, S. D. 2000, AJ, 119, 207
Lesch, H., & Reich, W. 1992, A&A, 264, 493
Matthews, B. C., Fiege, J. D., & Moriarty-Schieven, G. 2002, ApJ, 569, 304
Matthews, B. C., Wilson, C. D., & Fiege, J. D. 2001, ApJ, 562, 400
Morris, M., & Serabyn, E. 1996, ARA&A, 34, 645
Novak, G., Dotson, J. L., Dowell, C. D., Goldsmith, P. F., Hildebrand, R. H., Platt, S. R., & Schleuning, D. A. 1997, ApJ, 487, 320
Novak, G., Dotson, J. L., Dowell, C. D., Hildebrand, R. H., Renbarger, T., & Schleuning, D. A. 2000, ApJ, 529, 241
Novak, G., et al. 2003, ApJ, 583, L83
Okumura, S. K., Ishiguro, M., Kasuga, T., Morita, K., Kawabe, R., Fomalont, E. B., Hasegawa, T., & Kobayashi, H. 1991, ApJ, 378, 127
Pierce-Price, D., et al. 2000, ApJ, 545, L121
Plante, R. L., Lo, K. Y., & Crutcher, R. M. 1995, ApJ, 445, L113
Price, S. D., Egan, M. P., Carey, S. J., Mizuno, D. R., & Kuchar, T. A. 2001, AJ, 121, 2819
Schleuning, D. A. 1998, ApJ, 493, 811
Schleuning, D. A., Dowell, C. D., Hildebrand, R. H., & Platt, S. R. 1997, PASP, 109, 307
Serabyn, E., & Güsten, R. 1991, A&A, 242, 376

Serabyn, E., & Morris, M. 1994, ApJ, 424, L91

Serkowski, K. 1974, in Methods of Experimental Physics, Vol. 12: Part A: Astrophysics—Optical and Infrared, ed. N. Carleton (New York: Academic Press), 361

Sofue, Y., Reich, W., Inoue, M., & Seiradakis, J. H. 1987, PASJ, 39, 95

Staguhn, J., Stutski, J., Uchida, K. I., & Yusef-Zadeh, F. 1998, A&A, 336, 290

Tsuboi, M., Handa, T., Tabara, H., Kato, T., Sofue, Y., & Kaifu, N. 1986, AJ, 92, 818

Tsuboi, M., Handa, T., & Ukita, N. 1999, ApJS, 120, 1

Tsuboi, M., Ukita, N., & Handa, T. 1997, ApJ, 481, 263

Uchida, K. I., & Güsten, R. 1995, A&A, 298, 473

Uchida, Y., Shibata, K., & Sofue, Y. 1985, Nature, 317, 699

Yusef-Zadeh, F., & Morris, M. 1987a, AJ, 94, 1178

———. 1987b, ApJ, 320, 545

Yusef-Zadeh, F., Morris, M., & Chance, D. 1984, Nature, 310, 557

Yusef-Zadeh, F., Roberts, D. A., Goss, W. M., Frail, D. A., & Green, A. J. 1996, ApJ, 466, L25

Zylka, R., Mezger, P. G., & Wink, J. E. 1990, A&A, 234, 133